Preparation of Ni-doped ZnO ceramics for thermoelectric applications

H. Colder[*], E. Guilmeau, C. Harnois, S. Marinel, R. Retoux, E. Savary

CRISMAT, UCBN, ENSICAEN, 6 Boulevard du Maréchal Juin, 14050 Caen cedex, France

Abstract

$Zn_{1-x}Ni_xO$ dense ceramics were prepared from $Zn_{1-x}Ni_xO$ nanoparticles with x varying from 0 to 0.06. These nanoparticles were synthesized by liquid route. In the sintered samples, the solubility limit of Ni in the $Zn_{1-x}Ni_xO$ wurtzite structure was found to be 0.03. The increase of x until 0.03 led to a significant raise in both electrical conductivity (σ) and absolute value of Seebeck coefficient ($|S|$). Ni-richer samples ($x > 0.03$) contained in addition a small amount of Ni rich secondary phase (Zn_yNi_zO) with a cubic structure similar to NiO. The thermoelectric properties of all samples were investigated from room temperature to 1000 K. All doped samples showed a n-type semiconducting conductivity. For Ni contents higher than $x = 0.03$, the increase of the secondary phase content induced a decrease in σ and $|S|$. The highest power factor (0.6 mW m^{-1} K^{-2}) and ZT (0.09) were found for $Zn_{0.97}Ni_{0.03}O$ at 1000 K.

© 2011 Elsevier Ltd. All rights reserved.

Keywords: Nanocomposites; ZnO; Electrical conductivity; Thermal conductivity; Thermoelectric

1. Introduction

Thermoelectric energy conversion is a promising technology for both electrical power generation, in terms of waste heat recovery, and various electronic cooling devices. The efficiency of thermoelectric devices depends on material properties through the dimensionless figure of merit ZT where T is the working temperature. Z is defined as the ratio $\sigma S^2/\kappa$ with σ is the electrical conductivity, S is the Seebeck coefficient and κ is the thermal conductivity. The intermetallic materials like Bi_2Te_3 possess high thermoelectric performances.[1,2] But, they are easily decomposed or oxidized in air at high temperatures, thus applications are greatly limited. On the contrary, oxide materials are relatively stable at high temperatures. That is why they receive recent attention in the fields of energy conversion.[3]

Among the thermoelectric oxides, zinc oxide presents a large Seebeck coefficient and a high thermal stability and is in addition non-toxic.[4] It is a n-type semiconducting oxide with a wide band gap of 3.3 eV and crystallizes in a wurtzite structure with $a = 3.2488$ Å and $c = 5.2054$ Å.[5] Recent investigations on ZnO ceramics show that their thermoelectric properties can be improved by substitution with aluminum,[6–8] titanium,[9]

antimony[10] or nickel.[11] Up to now, only Park et al.[11] have studied Ni-doped ZnO ceramics for thermoelectric applications. Their ceramics were prepared by solid-state reaction, using ZnO and NiO as starting materials. Their best sample shows a power factor (PF) of 1.8 mW m^{-1} K^{-2} where the PF is defined as: $PF = \sigma S^2$. However, this conventional method of elaboration usually leads to heterogeneous distribution of the doping element. In addition, a relatively long sintering dwell time is often required. Indeed, the powder reactivity is low because of a quite large grain size distribution. In this work, we prepared Ni–ZnO powders by a liquid route, using inexpensive zinc and nickel acetate as starting materials. The liquid route is the optimal method to obtain powders with nanometer grain size. It usually leads to a homogeneous distribution of Ni through the ZnO lattice and to a decrease of both sintering time and temperature. The thermoelectric properties of the Ni–ZnO ceramics, synthesized by this procedure, were studied and discussed.

2. Experimental procedure

The $Zn_{1-x}Ni_xO$ nanoparticles for thermoelectric applications were prepared by liquid route synthesis, as described in previous work.[12] The zinc nickel acetate solution was obtained by the dissolution of zinc acetate dihydrate powder (Chempur 99.5%) in hot ethanol solution, followed by the dissolution of nickel acetate

* Corresponding author. Tel.: +33 2 31 45 13 68.
  E-mail address: heloise.colder@ensicaen.fr (H. Colder).

tetrahydrate. The proportion of nickel acetate was adjusted to obtain Ni atomic concentration from $x = 0$ to $x = 0.06$. Oxalic acid was added to precipitate the Zn–Ni oxalate. The dried powders were calcined in air at 450 °C for 2 h. The calcined powders were subsequently mixed by attrition in ethanol during 1 h 30. An organic binder (Rhodoviol 4%, Prolabo) was manually added to the dried powders. Finally, disks (diameter of 6 mm, thickness around 2 mm) and bars (12 mm × 3.3 mm × 3 mm) were shaped by using a 30.6 kN uniaxial load, before sintering.

The crystallized phases were identified by X-ray diffraction (XRD) using the Cu Kα radiation (Philips X'Pert diffractometer) and the crystalline parameters were determined by refinement with the least squares method using the JANA 2006 software.[13] The specific surface area of the powders was determined by the N_2 adsorption method using the Brunauer–Emmett–Teller (BET) equation. The crystallite size and morphology were characterized by transmission electron microscopy (TEM, Jeol). Thermo mechanical analysis (TMA, Setaram) was realized with a 5 K/min heating rate in air. Scanning electron microscopy (SEM) observations were done using a Zeiss Supra 55 and cationic composition was determined by electron dispersive spectroscopy (EDS) analysis (EDAX). Thermogravimetry (TG) and differential scanning calorimetry (DSC) measurements were performed on Setaram TGA92 system. Electrical conductivity (σ) and Seebeck coefficient (S) were measured by ZEM 3 (ULVAC-Riko) in order to determine the power factor (PF). Hall measurements were done to get the carrier concentration. Thermal conductivity (κ) was calculated from thermal diffusivity (λ) (LFA 457 Micro Flash) and specific heat capacity (Cp) (STA 449 F3 Jupiter). Finally, the merit factor (ZT) was deduced in the temperature range [300 K, 1000 K] by the relation: $ZT = \sigma S^2 T/\kappa$.

3. Results and discussion

3.1. ZnNiO nanoparticles

The DSC and TG curves of the oxalate precursors are shown in Fig. 1. From 100 °C to 250 °C, the weight loss and the endothermic peaks highlight the dehydration and the formation of the anhydrous oxalate. Beyond 400 °C, the exothermic peaks associated to a second weight loss suggest the decomposition of the anhydrous oxalate in mixed oxides as reported elsewhere.[14–16] In consequence, oxalate precursors were calcined at 450 °C for 2 h in air, with heating and cooling rates of 120 °C/h.

Fig. 2 shows the XRD patterns of the $Zn_{1-x}Ni_xO$ particles after calcination. All peaks are indexed in the wurtzite structure of ZnO (space group $P6_3mc$, JCPDF #89-0510). The broad peaks suggest that crystallites are nano-sized. This is confirmed by HRTEM observations that show spherical grains of 20 nm and a very narrow grain size distribution (Fig. 3). With spherical shape particles, the specific surface area measurements[12] give an average grain size of 28 nm for ZnO powder and 26 nm for $Zn_{0.97}Ni_{0.03}O$ powder. The crystallographic parameters a and c, deduced from XRD pattern simulation, do not show a significant dependence with the Ni content (Table 1). Hence, no clear
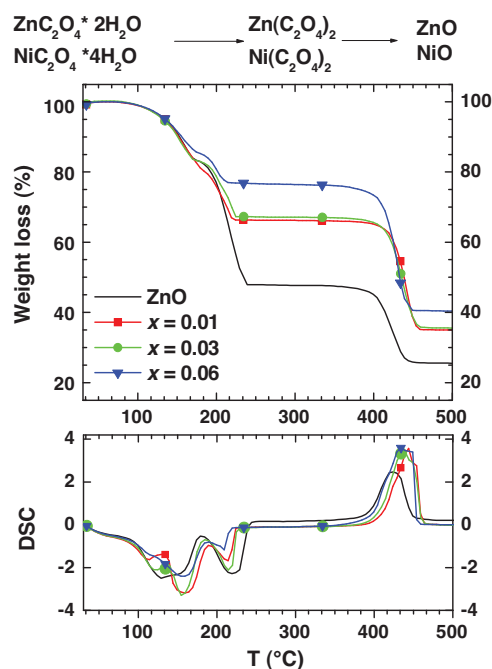

Fig. 1. The thermal analysis curves of Zn oxalate (straight line) and Zn–Ni oxalates for the following atomic fractions of Ni: $x = 0.01$ (■), $x = 0.03$ (●) and $x = 0.06$ (▼).
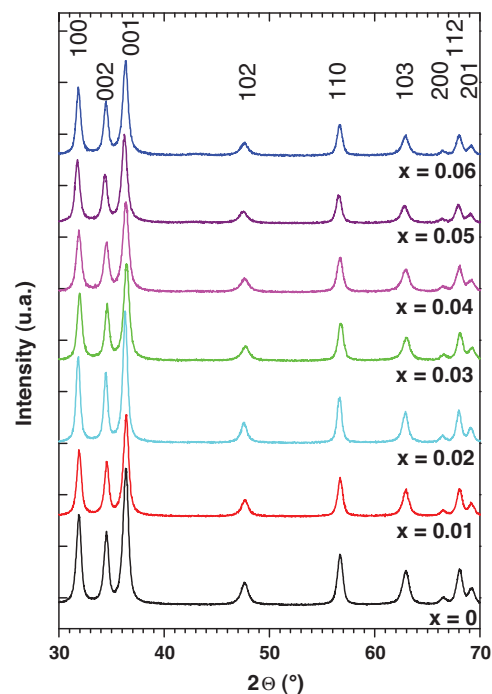

Fig. 2. X-ray diffraction patterns of $Zn_{1-x}Ni_xO$ nanoparticles with x varying from 0 to 0.06.

Table 1
Lattice parameters of the main wurtzite structure in the $Zn_{1-x}Ni_xO$ ($x = 0$, 0.03, 0.06) powders deduced from the XRD refinement.

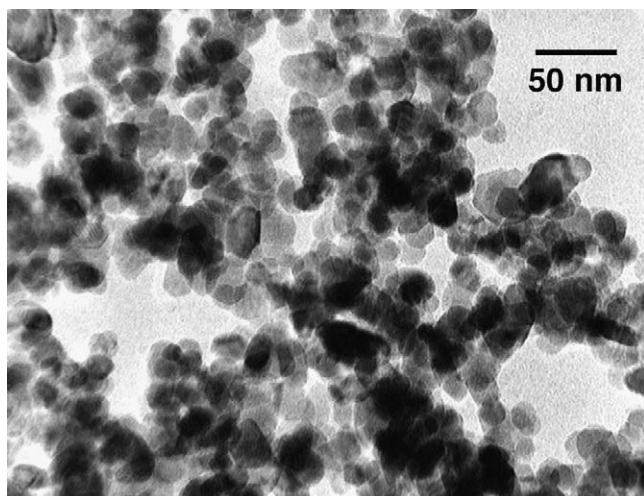| Name	a (Å)	c (Å)	V (Å^3)
ZnO	3.250 ± 0.003	5.211 ± 0.004	47.655 ± 0.006
$Zn_{0.97}Ni_{0.03}O$	3.250 ± 0.003	5.211 ± 0.005	47.657 ± 0.006
$Zn_{0.94}Ni_{0.06}O$	3.248 ± 0.003	5.209 ± 0.004	47.598 ± 0.006

Fig. 3. Typical shape and size distribution of ZnO dispersed nanoparticles.

influence of Ni content on the powder characteristics has been observed.

The TMA curves of $Zn_{1-x}Ni_xO$ for $x = 0$, 0.01, 0.03 and 0.06 are shown in Fig. 4. After sintering, the total shrinkage values range from 16 to 18%. For all samples, the shrinkage curves exhibit two steps. The first one (up to 1000 °C) corresponds to the rearrangement of the nanoparticles and the decrease of inter-particles distance. The second one corresponds to the sintering itself at high temperature. Therefore, all $Zn_{1-x}Ni_xO$ samples were sintered in air at 1400 °C during 2 h, with heating and cooling rates of 150 °C/h to ensure good densification.

3.2. $Zn_{1-x}Ni_xO$ ceramics

XRD patterns of $Zn_{1-x}Ni_xO$ sintered samples are shown in Fig. 5. The diffraction peaks can be indexed as the ZnO wurtzite phase with no impurity phase, except for $x = 0.05$ and $x = 0.06$ (see Fig. 5 inset). This impurity phase can be attributed either to NiO or to Zn_yNi_zO with cubic structure.[17–21] The lattice parameters a and c of the wurtzite phase have also been refined and are shown in Fig. 6. From $x = 0$ to $x = 0.03$, the increase in the a cell parameter is correlated to the decrease in the c cell parameter. The ratio c/a, estimated as 1.6016 for pure ZnO,
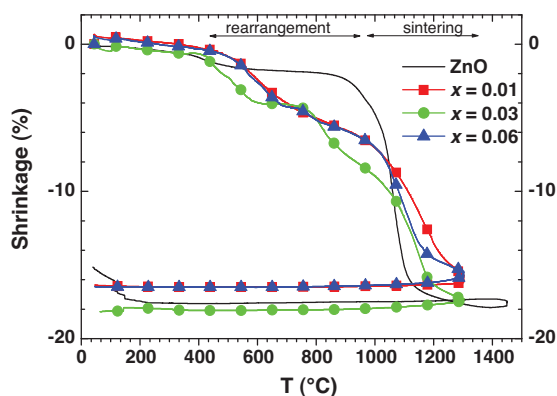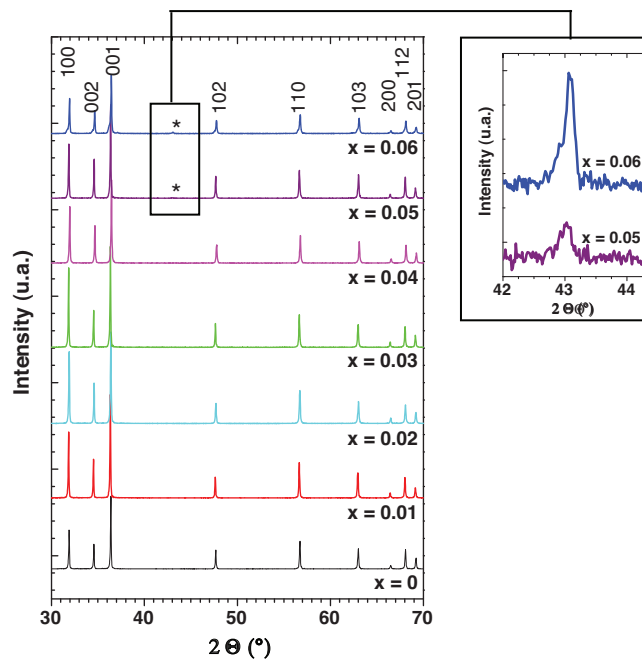

Fig. 5. X-ray diffraction pattern of $Zn_{1-x}Ni_xO$ samples with x varying from 0 to 0.06. The peaks of secondary phase is noted by * and an inset present a zoom on this particular zone.

falls down to 1.5995 for the $Zn_{0.97}Ni_{0.03}O$ composition. This behavior, already reported,[22–24] is explained by the partial occupation of Zn^{2+} sites by smaller Ni^{2+} ions, since the ionic radii of Zn^{2+} and Ni^{2+} are respectively 0.74 Å and 0.63 Å in tetrahedral coordination.[25] Beyond $x = 0.04$, no significant change is observed, indicating a solubility limit of Ni in ZnO close to $x = 0.03$. The solubility limit was also studied by the estimation of the Ni/Zn ratio determined by EDS. As shown in Fig. 7, for low Ni contents ($x \leq 0.03$), the ratio slightly changes from the theoretical ratio, and the most part of nickel substitutes Zn into the wurtzite structure. Beyond $x = 0.03$, the Ni/Zn ratio inside grain is almost stable, confirming a solubility limit around $x = 0.03$.

SEM micrographs of ZnO, $Zn_{0.97}Ni_{0.03}O$ and $Zn_{0.94}Ni_{0.06}O$ samples (see Fig. 8) evidence high densities and average grain size (estimated by the Mendelson approach[26]), of 30.5 μm,

Fig. 4. Shrinkage curves of the pellets of $Zn_{1-x}Ni_xO$ for $x = 0$, $x = 0.01$ (■), $x = 0.03$ (●) and $x = 0.06$ (▼).
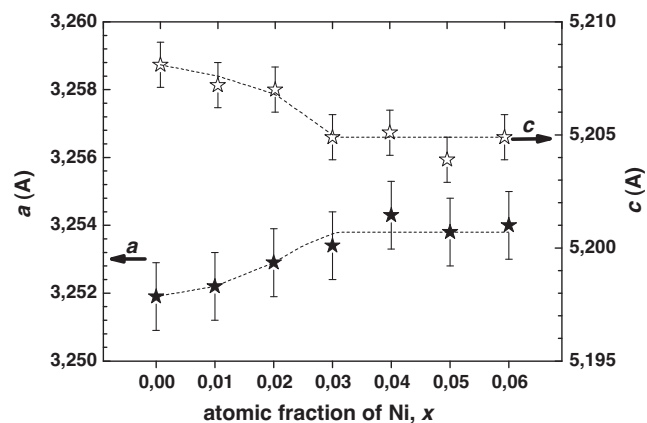

Fig. 6. Evolution of the lattice parameters (a and c) of the wurtzite structure in the $Zn_{1-x}Ni_xO$ sintered samples with x varying from 0 to 0.06.
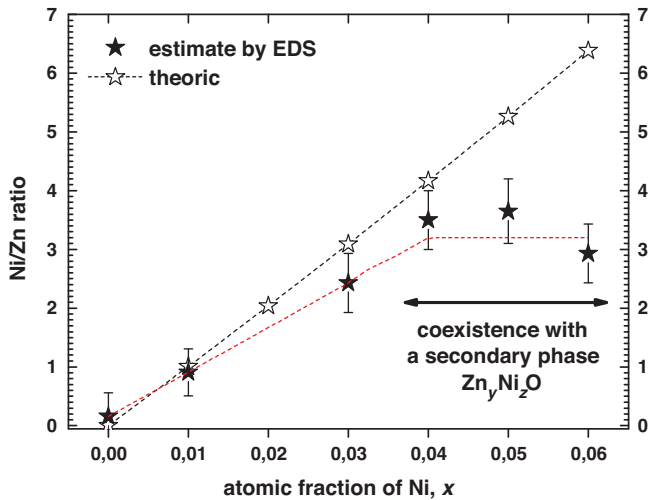
Fig. 7. Evolution of the Ni/Zn ratio evaluated from the atomic contents obtained by EDS versus x.

29 μm and 21 μm for $x = 0$, 0.03 and 0.06, respectively. For contents higher than 0.03, the grain size decrease may be explained by the presence of an intergranular secondary phase. This secondary phase limits the grain growth during sintering. Indeed, precipitates, which are localized at grain boundaries, often inhibit grain growth by decreasing the grain boundary mobility. EDS measurements performed by SEM and by TEM (not shown here) on this secondary phase reveal the presence of both Ni and Zn cations. Consequently, this phase is identified as a Ni rich secondary phase (Zn_yNi_zO) with a cubic structure similar to NiO.

3.3. Thermoelectric properties of ceramics

Fig. 9 shows the temperature dependence of (a) the electrical conductivity, (b) the Seebeck coefficient, (c) the power factor and (d) the thermal conductivity of $Zn_{1-x}Ni_xO$ compounds. For all the samples, the temperature dependence of the electrical conductivity exhibits a semiconducting behavior. The addition of Ni, up to $x = 0.03$, increases the conductivity by more than one order of magnitude at room temperature. The carrier concentration determined by Hall measurements is 1.6×10^{18} cm^{-3} for ZnO and 2.8×10^{19} cm^{-3} for $Zn_{0.97}Ni_{0.03}O$. The increase of σ can hence be mainly attributed to an increase in electron carrier concentration. As the presence of Ni^{3+} is unlikely,[21,27,28] the Ni^{2+} for Zn^{2+} homovalence substitution mainly occurs. But, in this configuration, the carrier concentration should not be changed. To explain this increase, we suggest that the Ni for Zn substitution may slightly change the ZnO band structure and add an impurity level in the bandgap. Indeed, a recent work of Singh et al.[29] proposes an explanation based on the impurity d-band splitting model induced by the crystal field and the Jahn–Teller effect. In ZnO, the Zn atoms are tetrahedral coordinated at four oxygen atoms. Under the influence of the field induced by oxygen, the d-states can be split into lower e_g states and higher t_{2g} states (see Fig. 10). The Jahn–Teller effect does not occur for pure ZnO as the Zn^{2+} d-states are full (d^{10}). However, in
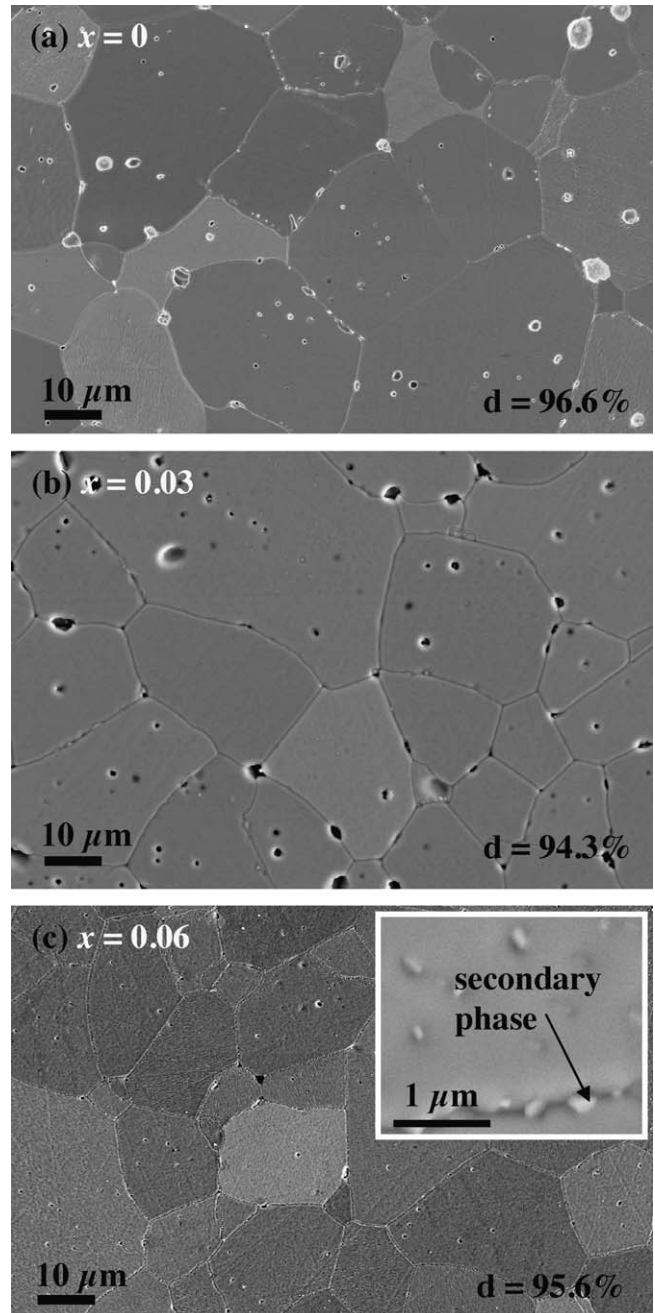

Fig. 8. SEM images of the sintered $Zn_{1-x}Ni_xO$ samples with $x = 0$ (a), $x = 0.03$ (b) and $x = 0.06$ (c).

the case of Ni^{2+}, the number of electron occupying the d-states is 8 (d^8). Therefore, when the Ni^{2+} is in tetrahedral environment, the Jahn–Teller effect may occur and the Ni-t_{2g} states are split into antibonding and bonding states. The t_{2g} antibonding states induce new energy levels, just below the conduction band. Thus, when temperature increases, the electrons of these states can jump to the conduction band and participate to the electrical conduction. This mechanism completely fits the experimental $\sigma(T)$ curves and the previously determined carrier concentration. When the Ni addition increases from $x = 0.03$ to $x = 0.06$, electrical conductivity decreases, as shown in Fig. 11. In Section 3.2, it has been shown that, for these Ni contents, a secondary
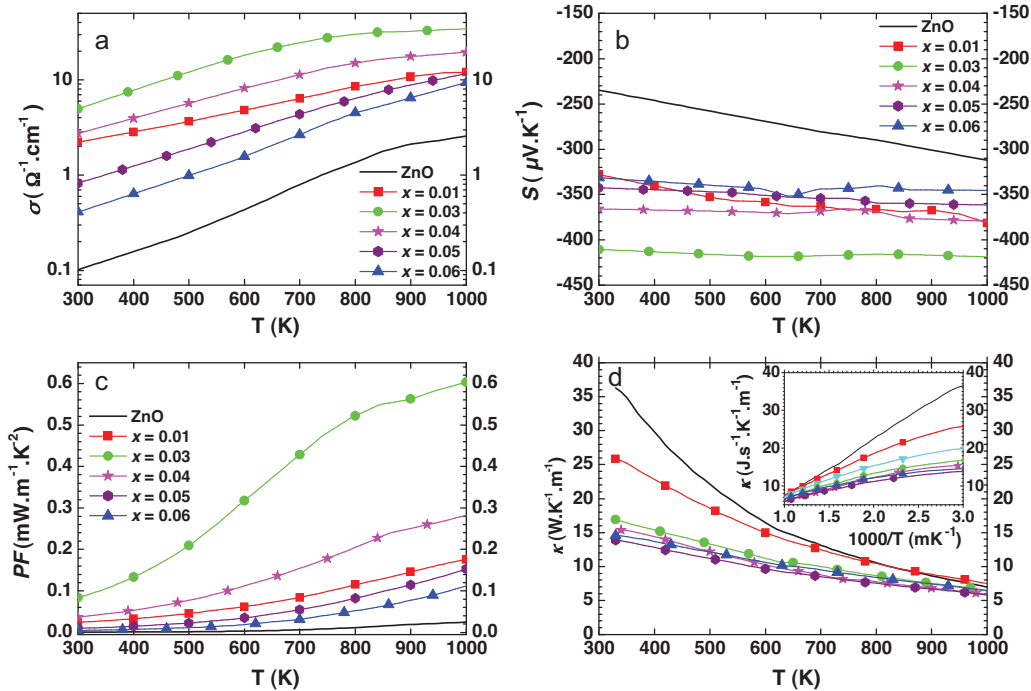
Fig. 9. Temperature dependence of the electrical conductivity σ (a), the Seebeck coefficient S (b), the power factor PF (c) and the thermal conductivity κ (d) of Ni doped ZnO and ZnO samples.
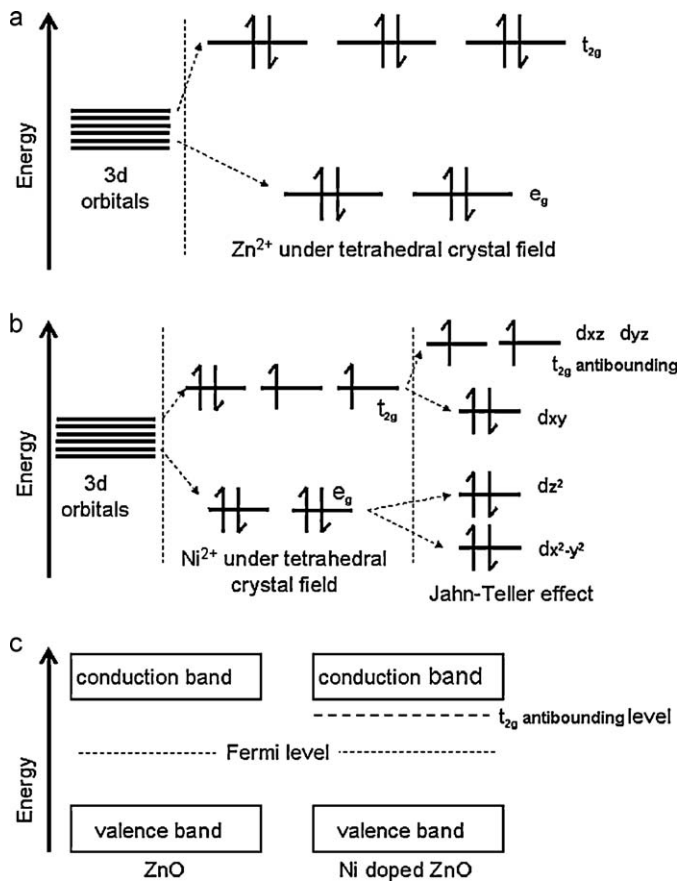

Fig. 10. (a) Zn^{2+} electronic structure under the crystal field of 4 oxygens. (b) Ni^{2+} electronic structure under the crystal field of 4 oxygens and under Jahn–Teller effect. (c) Bands structure of ZnO and Ni-doped ZnO.

phase appears in the vicinity of the grain boundary and that grain size decreases. These microstructural changes could explain the electrical conductivity decrease. Indeed, the grain size decrease involves the increase of the high resistive grain boundary surface.

In Fig. 9b, the Seebeck coefficient is negative over the whole temperature range for all the samples, which is in agreement with a conduction dominated by electron carriers. At room temperature the pure ZnO sample possesses a $|S|$ value of about $240 \, \mu V \, K^{-1}$, slightly higher than the one of other ZnO ceramics.[7,9–11,30] Only the ceramics obtained by Cheng et al.[6] present a higher value ($350 \, \mu V \, K^{-1}$).
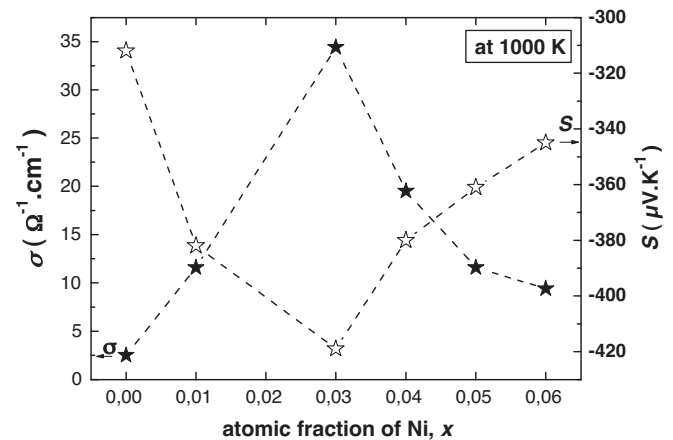

Fig. 11. Evolution of the electrical conductivity σ, the Seebeck coefficient S, at 1000 K versus x.

According to a simplified broadband model, S of the extrinsic n-type semiconductor with negligible holes conduction can be expressed as follows (Eq. (1))[31]:

$$S = -\frac{k_B}{q}\left(\ln\left(\frac{N_c}{n}\right) + A\right) \tag{1}$$

where k_B is Boltzmann constant, q is the electron charge, N_c refers to the density of state, n denotes carrier concentration and A is a transport constant. According to this equation, the increase in the carrier concentration could lead to a lowered $|S|$. In our case, it has been clearly seen that the Ni-additions (up to $x = 0.03$) induces a slight n increasing. Because of that, a decrease in $|S|$ is expected with Ni content increase. Actually, we observe the opposite (Fig. 11). This unusual evolution of S and σ has been already observed in Sb doped ZnO[10] and in Ca doped CuAlO$_2$.[32]

When the Ni content increases from $x = 0.03$ to $x = 0.06$, $|S|$ decreases. This is in agreement with the appearance of the secondary phase, usually exhibiting positive Seebeck coefficient of $\sim 100\,\mu V\,K^{-1}$.[33]

The power factor, expressed by $PF = \sigma S^2$, is plotted in Fig. 9c. In the whole temperature range, the PF is improved by the Ni-addition up to $x = 0.03$, since both σ and $|S|$ increase. Beyond $x = 0.03$, PF decreases with the Ni addition mainly due to the presence of the secondary phase that induces a decrease in both σ and $|S|$. In consequence, the highest value of the PF is $0.56\,mW\,m^{-1}\,K^{-2}$ at 900 K, for Zn$_{0.97}$Ni$_{0.03}$O. This sample is composed of a (Ni,Zn)O solid solution single phase. This PF value is of the same order of magnitude than the PF reported by Park,[11] concerning samples with the same composition, but sintered 8 times longer. Moreover, at this working temperature, Ni seems to be more efficient than Ti ($PF \leq 0.4\,mW\,m^{-1}\,K^{-2}$),[9] Sb ($PF \leq 0.175\,mW\,m^{-1}\,K^{-2}$)[10] or Al ($PF \leq 0.35\,mW\,m^{-1}\,K^{-2}$).[6]

The variation of thermal conductivity κ with temperature for the various samples is shown in Fig. 9d. The wurtzite ZnO has a high intrinsic thermal conductivity. In single crystal, the κ value can be as high as $100\,W\,m^{-1}\,K^{-1}$.[6] For $x = 0$, the room temperature thermal conductivity is estimated in the present work around $37\,W\,m^{-1}\,K^{-1}$, a value which is similar to other reported results.[6,7,30] With x from 0.01 to 0.03, κ goes down to $17\,W\,m^{-1}\,K^{-1}$. For $x \geq 0.03$, it remains stable, being independent on nickel content.

As observed in Fig. 9d, increase in temperature steadily reduces the thermal conductivity for all samples. As shown on the inset, a linear relationship can be found in the κ ($10^3/T$) curve indicating that κ is dominated by phonon transfer.[6] It is also noted that, at low temperature, the κ values of Ni-added ZnO samples are lower than the κ of ZnO sample. This agrees with the theoretical prediction that, at low temperature, grain boundary and impurity scattering dominate phonon transfer and determine the final thermal conductivity.

The dimensionless figure of merit ZT has been calculated, with the formula $ZT = \sigma S^2 T/\kappa$. The temperature dependence of ZT is plotted in Fig. 12. The results show that Ni addition helps to improve the ZT of ZnO material, especially at high temperatures. The highest value of 0.09 is obtained for the composition
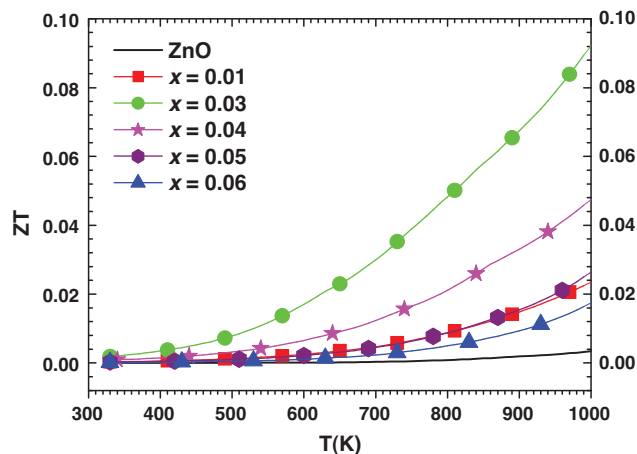

Fig. 12. Temperature dependence of the figure of merit ZT of ZnO and Ni-doped ZnO samples.

Zn$_{0.97}$Ni$_{0.03}$O, at 1000 K. This value is lower than the 0.2 value of the ZT reported by Otaki et al.[8] concerning Zn$_{0.98}$Al$_{0.02}$O at 1073 K and higher than ~ 0.035, at 1000 K, reported by Cheng et al.[6] about Zn$_{0.99}$Al$_{0.01}$O. Moreover, at 700 K, Cai et al. referred of values of ZT of 0.024 and 0.015 about the TiB$_2$–ZnO composites and Al-doped ZnO, respectively[7,30] whereas Ni doped ZnO exhibits a better ZT of 0.03 at this temperature. Hence, the Zn$_{0.97}$Ni$_{0.03}$O ceramics elaborated by liquid route seem to be good candidate for TE applications, in high working temperature range. Furthermore, the thermoelectric properties can be improved by introducing a co-doping with Al, which should increased the conductivity as in Al and Ni co-doped ZnO films.[34]

4. Conclusions

The Zn$_{1-x}$Ni$_x$O ($x \leq 0.06$) oxide ceramics were prepared by liquid route and conventional sintering. The samples with x values below 0.03 show a dense microstructure of a single phase with wurtzite ZnO structure, whereas the other samples present a secondary phase identified as cubic (Zn$_y$Ni$_z$O). It is found that the substitution of Zn by Ni in ZnO until 3 at.% increases higher x values, the opposite behavior was observed. Therefore, the PF was optimized for $x = 0.03$ reaching a value of $0.56\,mW\,m^{-1}\,K^{-2}$ at 900 K. It also shows that the doped element is effective in reducing the thermal conductivity at room temperature. Finally, the enhanced ZT values were obtained in the composition Zn$_{0.97}$Ni$_{0.03}$O (0.09 at 1000 K).

References

1. Poudel B, Hao Q, Ma Y, lan YC, Minnich A, Yu B, Yan X, Wang DZ, Muto A, Vashae D, Chen XY, Liu JM, Dresselhaus MS, Chen G, Ren Z. *Science* 2008;**320**:634–8.

2. Li JF, Liu J. *Phys Stat Sol A* 2006;**203**:3768–73.

3. Li F, Li J-F. *Ceram Int* 2011;**37**:105–10.

4. Souma T, Ohtaki M, Shigeno M, Ohba Y, Nakamura N, Shimozaki T. *Thermoelectrics IEEE* 2006:603–6.

5. Sawada H, Wang R, Sleight AW. *J Solid State Chem* 1996;**122**:148–50.

6. Cheng H, Xu XJ, Hng HH, Ma J. *Ceram Int* 2009;**35**:3067–72.

7. Cai KF, Müller E, Drasar C, Mrotzek A. *Mater Sci Eng B* 2003;**104**:45–8.

8. Otaki M, Tsubota T, Eguchi K, Arai H. *J Appl Phys* 1996;**79**:1816.

9. Park K, Ko KY. *J Alloys Compd* 2007;**430**:200–4.

10. Park K, Seong JK, Nahm S. *J Alloys Compd* 2008;**455**:331–5.

11. Park K, Seong KY, Kim GH. *J Alloys Compd* 2009;**473**:423–7.

12. Savary E, Marinel S, Colder H, Harnois C, Lefèvre FX, Retoux R. *Power Technol* 2009.

13. Petricek V, Dusek M, Palatinus L. *Jana2006. The crystallographic computing system*. Praha, Czech Republic: Institute of Physics; 2006.

14. Andrew M, Galwey K, Halawy S. *Thermochim Acta* 2005;**429**:57–72.

15. Cong CJ, Hong JH, Liu QY, Liao L, Zhang KL. *Solid State Commun* 2006;**138**(10-11):511–5.

16. Salavati-Niasari M, Mir N, Davar F. *Polyhedron* 2009;**28**(6):1111–4.

17. Pandey B, Ghosh S, Srivastava P, Kabiraj D, Shripati T, Lalla NP. *Physica E* 2009:1164–8.

18. Kim KT, Kim GH, Woo JC, Kim CI. *Surf Coat Technol* 2008;**202**:5650–3.

19. Triboulet R, Perrière J. *Prog Cryst Growth Charact Mater* 2003;**47**:65–138.

20. Xu J, Yang H, Fu W, Fan W, Zhu Q, Li M, Zou G. *J Alloys Compd* 2008;**458**:119–22.

21. Gayen RN, Rajaram A, Bhar R, Pal AK. *Thin Solid Films* 2010;**518**:1627–36.

22. El-Hilo M, Dakhel AA, Ali-Mohamed AY. *J Magn Magn Mater* 2009;**321**:2279–83.

23. Thota S, Kukreja LM, Kumar J. *Thin Solid Films* 2008;**517**:750–4.

24. Wakano T, Fujimura N, Morinaga Y, Abe N, Ashida A, Ito T. *Physica E* 2001:260–4.

25. Shannon RD. *Acta Crystallogr A* 1976;**32**:751–6.

26. Mendelson MI. *J Am Ceram Soc* 1969;**52**:445–6.

27. Shing S, Rama N, Ramachandra Rao MS. *Appl Phys Lett* 2006;**88**:222111.

28. Ghosh S, Srivastava P, Pandey B, Sauray M, Bharadwaj P, Avasthi DK, Kabiraj D, Shivaprasad SM. *Appl Phys A* 2008;**90**(76):5–769.

29. Singh S, Rama N, Sethupathi K, Ramachandra Rao MS. *J Appl Phys* 2008;**103**, 07D108.

30. Cai KF, Müller E, Drasar C, Mrotzek A. *Mater Lett* 2003:4251–5.

31. Wiff JP, Kinemuchi Y, Kaga H, Ito C, Watari K. *J Eur Ceram Soc* 2009;**29**:1413–8.

32. Park K, Ko KY, Seo WS. *Mater Sci Eng B* 2006;**129**:1–7.

33. Shin W, Murayama N. *Mater Lett* 2000;**45**:302–6.

34. Yu M, Qiu H, Chen X, Li H, Gong W. *Mater Chem Phys* 2010;**120**: 571.